The Dense Gas Fraction in Galactic Center Clouds

E. A. C. Mills[1] , A. Ginsburg[2,7] , K. Immer[3], J. M. Barnes[2,8], L. Wiesenfeld[4], A. Faure[4] , M. R. Morris[5] , and
M. A. Requena-Torres[6]

[1] Physics Department, Brandeis University, 415 South Street, Waltham, MA 02453, USA; elisabeth.ac.mills@gmail.com
[2] National Radio Astronomy Observatory,[9] 1003 Lopezville Rd., Socorro, NM 87801, USA
[3] Joint Institute for VLBI ERIC, Oude Hoogeveensedijk 4 7991 PD, Dwingeloo, The Netherlands
[4] Université Grenoble Alpes, CNRS, IPAG, F-38000 Grenoble, France
[5] Department of Physics and Astronomy, University of California, Los Angeles, 430 Portola Plaza, Box 951547, Los Angeles, CA 90095-1547, USA
[6] Department of Astronomy, University of Maryland, College Park, MD 20742, USA

Abstract

We present an analysis of gas densities in the central $R = 300$ pc of the Milky Way, focusing on three clouds: GCM –0.02–0.07 (the $50 \, \mathrm{km \, s^{-1}}$ cloud), GCM –0.13–0.08 (the $20 \, \mathrm{km \, s^{-1}}$ cloud), and GCM 0.25+0.01 (the "Brick"). Densities are determined using observations of the $J = (3–2)$, $(4–3)$, $(5–4)$, $(10–9)$, $(18–17)$, $(19–18)$, $(21–20)$, and $(24–23)$ transitions of the molecule HC_3N. We find evidence of at least two excitation regimes for HC_3N and constrain the low-excitation component to have a density less than $10^4 \, \mathrm{cm^{-3}}$ and the high-excitation component to have a density between 10^5 and $10^6 \, \mathrm{cm^{-3}}$. This is much less than densities of $10^7 \, \mathrm{cm^{-3}}$ that are found in Sgr B2, the most actively star-forming cloud in the Galactic center. This is consistent with the requirement of a higher-density threshold for star formation in the Galactic center than is typical in the Galactic disk. We are also able to constrain the column density of each component in order to determine the mass fraction of "dense" $(n > 10^5 \, \mathrm{cm^{-3}})$ gas for these clouds. We find that this is ∼15% for all three clouds. Applying the results of our models to ratios of the (10–9) and (3–2) line across the entire central $R = 300$ pc, we find that the fraction of dense $(n > 10^4 \, \mathrm{cm^{-3}})$ gas increases inward of a radius of ∼140 pc, consistent with the predictions of recent models for the gas dynamics in this region. Our observations show that HC_3N is an excellent molecule for probing the density structure of clouds in the Galactic center.

Key words: Galaxy: center – ISM: abundances – ISM: clouds – ISM: molecules – radio lines: ISM

1. Introduction

The inner $R \sim 300$ pc of the Milky Way hosts a concentration of molecular gas known as the Central Molecular Zone or "CMZ." Slightly less than 5% of the total molecular gas reservoir of ∼$8.4 \times 10^8 \, M_\odot$ in the Galaxy is estimated to be contained in this region (Dahmen et al. 1998; Nakanishi & Sofue 2006). In the Milky Way's CMZ, the bulk of the gas at high column density is found in a ring of giant molecular clouds, orbiting the central supermassive black hole at radii of 50–100 pc (Molinari et al. 2011; Kruijssen et al. 2015), on so-called "x2" orbits (Binney et al. 1991). Recent theory predicts that gas accumulates at these radii owing to a minimum in the shear that is responsible for its radial transport (Krumholz & Kruijssen 2015). Similarly sized and shaped central concentrations of gas are frequently seen in the centers of barred galaxies, including nearby galaxies like IC 342 (Ishizuki et al. 1990), M83 (Elmegreen et al. 1998), the starburst NGC 253 (García-Burillo et al. 2000), and the Seyfert 2 galaxy NGC 4945 (Chou et al. 2007). In the CMZ, the distribution of this gas is asymmetric in several ways, with more gas found both at positive longitudes and on the near side of this ring, which is suggested to be due to some combination of instabilities in inflowing gas (Sormani et al. 2018) and tidal compression at different points along the orbit (Longmore et al. 2013b).

Inside the CMZ, the properties of the gas are much more extreme than in the Galactic disk. Gas temperatures are measured to range from 50 to 400 K (Güsten et al. 1985; Hüttemeister et al. 1993; Ao et al. 2013; Mills & Morris 2013; Ginsburg et al. 2016; Krieger et al. 2017), significantly elevated over the dust temperatures, which range from 20 to 50 K (Molinari et al. 2011; Longmore et al. 2012, C. Battersby et al. 2018, in preparation). Line widths due to turbulent motions are also large, with σ ranging from 0.6 to $20 \, \mathrm{km \, s^{-1}}$ over size scales of 0.2–2 pc (Montero-Castaño et al. 2009; Shetty et al. 2012; Kauffmann et al. 2017), though it should be noted that on scales $\gtrsim 0.5$ pc, some of these large line widths are also due to coherent velocity gradients from both orbital motion and strong shearing (e.g., Federrath et al. 2016). Finally, as a result of either the increased temperature or turbulence (or both), the gas is also extremely chemically rich, with "hot core" molecules widespread and abundant in this region (Requena-Torres et al. 2006; Jones et al. 2012, 2013). The elevated densities and temperatures, as well as the rich chemistry seen in the CMZ, are similar to conditions observed in the nuclei of nearby galaxies like NGC 253, IC 342, and Maffei 2 (Paglione et al. 1995; Henkel et al. 2000; Meier & Turner 2005, 2012; Ott et al. 2005; Meier et al. 2015; Gorski et al. 2017, 2018).

Gas densities are also higher than those found in the disk, with the average density in the CMZ canonically taken to be $10^4 \, \mathrm{cm^{-3}}$ (Güsten & Henkel 1983; Bally et al. 1987) and values for different gas components ranging from 10^2 to $10^7 \, \mathrm{cm^{-3}}$ (Walmsley et al. 1986; Lis & Goldsmith 1991; Dahmen et al. 1998; Magnani et al. 2006; Etxaluze et al. 2011; Goto et al. 2011; Requena-Torres et al. 2012; Mills et al. 2013). However, the various methods used to determine gas densities

---

have key uncertainties. Density measurements based on the critical density of individual molecular transitions (e.g., Bally et al. 1987; Longmore et al. 2013a) can be significantly in error based on the actual gas excitation conditions (Shirley 2015). Gas densities inferred from column densities depend sensitively on an assumption of 3D shape, which can lead to errors if clouds are elongated along the line of sight (Longmore et al. 2012; Henshaw et al. 2016). Excitation-derived gas densities have the potential to be more accurate than either of these methods. However, in practice these are often subject to significant uncertainties due to the degeneracy between temperature and density in driving the excitation for most molecules (Dahmen et al. 1998). Moreover, nearly all estimates of density derived from excitation apart from those determined toward a few exceptional sources (e.g., the CND and Sgr B2; Lis & Goldsmith 1991; Requena-Torres et al. 2012; Mills et al. 2013) have assumed that there is only a single density component present in the gas (Güsten & Henkel 1983; Serabyn & Güsten 1991; Serabyn et al. 1992; Zylka et al. 1992; Tanaka et al. 2018). Thus, the distribution of gas densities in the CMZ and the density structure of individual clouds are both poorly constrained.

Measurements of cloud density are especially pertinent for understanding why the Galactic center has so little star formation ($\sim$5% of the total star formation rate of the Milky Way as a whole; Yusef-Zadeh et al. 2009; Chomiuk & Povich 2011; Crocker 2012; Longmore et al. 2013a; Koepferl et al. 2015). While this might appear consistent with the fraction of the Galaxy's molecular gas that lies in the CMZ (also $\sim$5%), the large fraction of gas in this region that is "dense" ($n > 10^4$) appears to violate "laws" relating the amount of gas to the amount of star formation (Lada et al. 2013; Longmore et al. 2013a). Determining whether the CMZ is truly a discrepant point in these universal relationships (e.g., a universal threshold of gas density needed to form stars anywhere in a galaxy may not be valid in an environment like the Galactic center with much stronger shear or larger turbulence; Kruijssen et al. 2014) first requires a careful assessment of whether we are undercounting the amount of star formation (e.g., Lu et al. 2017) or overestimating the dense gas fraction.

We present measurements of density in three CMZ clouds, GCM –0.02–0.07, GCM –0.13–0.08 (the 50 and 20 km s^{-1} clouds in the Sgr A complex), and GCM 0.25+0.01 (the so-called "Brick" cloud in the dust ridge between Sgr A and Sgr B2), using multiple transitions of HC$_3$N. In the high column density environment of the CMZ, the relatively low abundance of HC$_3$N relative to H$_2$ ($\sim$3 × 10^{-8}, assuming a CO-to-H$_2$ abundance of 10^{-4}; Walmsley et al. 1986) makes it an optically thin tracer, as opposed to molecules like CO and HCN, which become optically thick or self-absorbed (Dahmen et al. 1998; Mills & Battersby 2017). Additionally, as a relatively heavy molecule HC$_3$N has closely spaced rotational transitions, allowing for efficient observation of transitions spanning a huge range of critical densities. Finally, HC$_3$N has a simple, linear structure, with well-determined collisional coefficients calculated up to temperatures of 300 K, appropriate for the Galactic center environment (Faure et al. 2016). This makes HC$_3$N an ideal tracer for measuring density structure in CMZ clouds. In Section 2 we describe the setup of observations used in our analysis. The measured parameters of the HC$_3$N emission and our excitation modeling are presented in

Table 1
Observed Transitions of HC$_3$N

Transition	Frequency (GHz)	E_{upper}/k (K)	n_{crit} at 50 K[a] ($\times 10^4$ cm^{-3})	Telescope	Beam FWHM (arcsec)
H^{13}CCCN					
(3–2)	26.450591	2.5		GBT	28
(5–4)	44.084162	6.3		GBT	17
HC$_3$N					
(3–2)	27.29429	2.6	0.18	GBT	28
				Mopra	120
(4–3)	36.39232	4.2	0.47	GBT	21
(5–4)	45.49031	6.5	0.96	GBT	17
				Mopra	65
(10–9)	90.97902	24.0	8.2	Mopra	40
(18–17)	163.75339	74.7	190	APEX	38
(19–18)	172.84930	83.0	220	APEX	38
(21–20)	191.04030	100.9	280	APEX	38
(24–23)	218.32472	131.0	$\sim$590	APEX	29

Note.
[a] Calculated using the collisional coefficients of Faure et al. (2016).

Section 3. We conclude in Section 4 with a discussion of the derived densities and their relevance to understanding star formation in the CMZ environment.

2. Observations and Data Calibration

The data used in the density analysis in this paper were obtained from three sources: the 100 m Green Bank telescope (GBT) of the Green Bank Observatory,[10] the 22 m Mopra radio telescope in Australia, and the 12 m Atacama Pathfinder EXperiment (APEX) telescope in Chile.
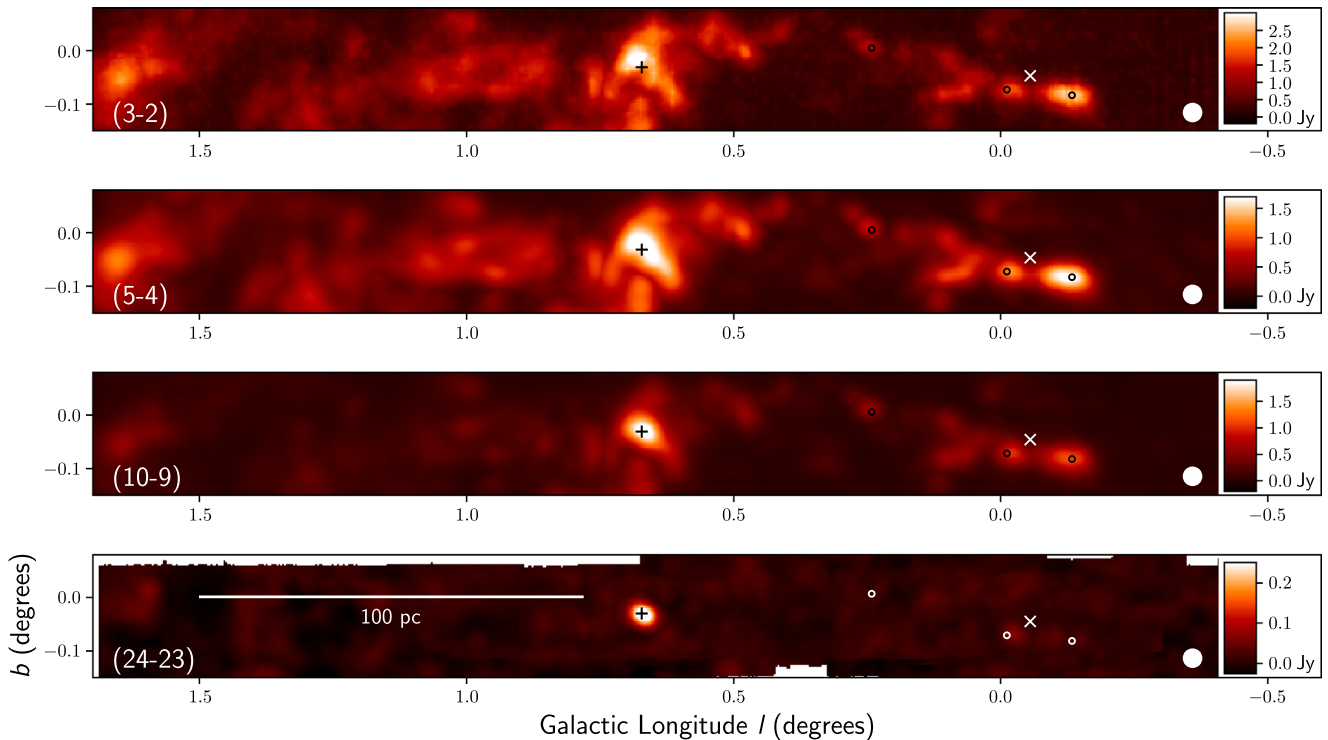
In total, eight rotational transitions of HC$_3$N were observed: $J =$ (3–2), (4–3), (5–4), (10–9), (18–17), (19–18), (21–20), and (24–23). We also observed the ^{13}C isotopologues of HC$_3$N in the $J =$ (3–2) and (5–4) transitions. Properties of all observed transitions including rest frequencies are given in Table 1.

2.1. Mopra

Maps of HC$_3$N emission are available from several surveys conducted with the Mopra radio telescope. HC$_3$N (10–9) and (5–4) line maps were taken from CMZ surveys published in Jones et al. (2012) and Jones et al. (2013). These lines were observed over a 2.5 × 0.5 deg^2 region covering the inner 350 pc of the CMZ (assuming a galactocentric distance of 8 kpc; Boehle et al. 2016) and including all three of the clouds studied here. HC$_3$N (3–2) line maps were taken from the HOPS southern Galactic plane survey (Walsh et al. 2011). The description of the data calibration is given in the survey papers. Calibrated and imaged survey data were obtained from the Australia Telescope Online Archive.[11] The (10–9) data have a spatial resolution of 40$''$, a velocity resolution of $\sim$2 km s^{-1}, and a per-channel rms noise of 50 mK. The (5–4) data have a spatial resolution of 65$''$, a velocity resolution of $\sim$1.8 km s^{-1}, and a per-channel rms noise of 37 mK. The (3–2) data have a

[11] https://atoa.atnf.csiro.au/

Figure 1. Maps of peak emission in the CMZ for the $J = (3–2)$, $(5–4)$, $(10–9)$, and $(24–23)$ transitions of HC_3N, smoothed to a $120''$ beam. The size of the smoothed beam is shown as a filled white circle. The white cross marks the location of Sgr A*, and the black cross marks the location of Sgr B2(N). Circles indicate the positions for which there are additional, pointed observations made with the GBT in the $J = (3–2)$, $(4–3)$, and $(5–4)$ lines.

spatial resolution of $120''$, a velocity resolution of $\sim 0.4\ km\ s^{-1}$, and a per-channel rms noise of 200 mK. Integrated emission maps of all these lines in the CMZ are shown in Figure 1. The estimated uncertainty of the amplitude calibration of these data is $<25\%$.

2.2. GBT

We have also made pointed observations of the HC_3N (3–2), (4–3), and (5–4) transitions with the GBT as part of a survey for highly excited NH_3 emission published in Mills & Morris (2013). The data were observed with the dual-beam Ka-band and Q receivers between 2009 May 12 and 29. We employed a position-switching technique, using an offset position of (R.A., decl.) = $(17^h46^m00^s, -28°13'57'')$ for clouds east of $l = 0°.1$ and an offset position of (R.A., decl.) = $(17^h45^m59^s.9, -29° 16'\ 47'')$ for more westerly clouds. With the GBTIDL[12] reduction and analysis software, we corrected the antenna temperature of the observed targets for the frequency-dependent opacity at the observed elevation. We also used observations of the flux calibrator 3C 286 to more accurately determine the relative amplitude calibration of the data, which is otherwise limited to 10%–15% accuracy by the temporal fluctuations of the noise diode. We estimate the uncertainty of our relative amplitude calibration to be $<10\%$ based on the rms fluctuations in the observed spectrum of the phase calibrator. Finally, we assumed that the observed emission is extended over an area larger than the telescope beam, and we applied a frequency-independent correction of 1.32 for the main-beam efficiency. Additional details pertaining to the observations and calibration of these data are given in Mills & Morris (2013).

Observations of all lines observed with the GBT were made in a single, pointed beam toward each cloud. For GCM 0.25+0.01, the pointing was centered on (R.A., decl.) = $(17^h46^m10^s.3, -28°43'37''.0)$. For GCM –0.02–0.07, the pointing was centered on (R.A., decl.) = $(17^h45^m52^s.4, -28° 59'02''.0)$. For GCM –0.13–0.08, the pointing was centered on (R.A., decl.) = $(17^h45^m37^s.9, -29°03'52''.0)$. The spatial resolution of the data ranged from $17''$ for the (5–4) line to $28''$ for the (3–2) line. The spectral resolution of the observations was 390.625 kHz, or $3.1–4.4\ km\ s^{-1}$ over the observed range of frequencies, sufficient to resolve lines with intrinsic widths of $15–30\ km\ s^{-1}$. The positions of these pointings are shown in Figure 1.

Finally, for the GCM –0.02–0.07 cloud, a $4' \times 4'$ map centered on (R.A., decl.) = $(17^h45^m52^s, -28°59'03'')$ was also observed using the GBT in the $HC_3N\ J = (5–4)$ line.

2.3. APEX

Observations of the HC_3N (24–23) line were made with the 230 GHz facility receiver. These observations composed a $120' \times 16'$ map of the entire 300 pc inner region of the CMZ as part of the observations presented in Ginsburg et al. (2016). Details of these observations and the procedures for calibration and imaging are given in this paper. The spatial resolution of these data is $\sim 29''$, and the velocity resolution is $1\ km\ s^{-1}$. The per-channel rms noise near the HC_3N (24–23) line is ~ 0.03 K. The estimated uncertainty of the amplitude calibration of these data is $\sim 15\%$.

Observations of the HC_3N (18–17), (19–18), and (21–20) lines were also made with the SEPIA receiver (Belitsky et al. 2018) covering small mosaics toward the three clouds studied here. The spatial resolution of these data is $\sim 38''$, and

the velocity resolution is 1 km s^{-1}. The per-channel rms noise near the observed HC$_3$N lines is 0.01–0.02 K. The estimated uncertainty of the amplitude calibration of these data is ∼10%.

2.4. Data Combination

The data set studied in this paper consists of a combination of maps and pointed observations toward GCM 0.25+0.01, GCM − 0.02–0.07, and GCM − 0.13–0.08. We conduct two separate analyses. The first is a study of the emission from all eight HC$_3$N transitions in a single beam toward the three clouds. For this analysis, we do not use maps of the (3–2) or (5–4) line, and we smooth all other maps to the lowest common spatial resolution (40″), set by the $J = (10–9)$ observations. For these map data, the $J = (10–9)$ line observed with Mopra, and the $J = (18–17)$, (19–18), (21–20), and (24–23) lines observed with APEX, spectra are extracted for each cloud at the position of the GBT observations. As the GBT data consist of single pointings toward these positions, the resolution of the (5–4) and (4–3) line data cannot generally be perfectly matched to that of the other data sets. As a result, we estimate a larger uncertainty for these measurements. However, for the GCM −0.02–0.07 cloud, which was mapped with the GBT in the $J = (5–4)$ line, a spectrum for this line can be extracted from a 40″ aperture to match the resolution of the lines extracted from the other maps.

For the second analysis, we study the ratio of HC$_3$N lines over the entire CMZ using maps of the (3–2), (5–4), and (10–9) lines. For this analysis, all maps are smoothed to the resolution of the (3–2) line (120″).

3. Results and Analysis

The spectra of all of the HC$_3$N lines observed toward each source are displayed in Figures 2 and 3. Toward GCM 0.25+0.01, all eight main transitions of the main isotopologue of HC$_3$N are observed and detected, as well as the two transitions of H^{13}CCCN. Toward GCM −0.02–0.07 and GCM–0.13–0.08, we do not have observations of the HC$_3$N (4–3) line, but all other lines are observed and detected. For all detected transitions, we fit the spectral lines with Gaussian profiles using PySpecKit (Ginsburg et al. 2011).

The spectra toward GCM −0.02–0.07 show a single velocity component at ∼48 km s^{-1}, which we are able to fit with a single Gaussian profile having a width of ∼22 km s^{-1}. However, the spectra toward GCM −0.13–0.08 and GCM 0.25+0.01 are somewhat more complicated, with each of these showing two discernible velocity components in many of the observed spectra. For these two clouds, we then fit up to two Gaussian profiles to their line spectra. For GCM −0.13–0.08, there is a primary velocity component with FWHM ∼ 18 km s^{-1} centered at ∼7 km s^{-1} and a second, narrower velocity component (FWHM ∼ 6 km s^{-1}) at ∼12 km s^{-1} that is prominent in lines with $J \lesssim 5$. We therefore fit both of these components in the $J = (3–2)$, (4–3), and (5–4) lines of HC$_3$N and H^{13}CCCN, but we only fit a single component in the higher-J lines. For GCM 0.25+0.01, there is a weak, low-velocity component at ∼20 km s^{-1} and a stronger, main line component at ∼35 km s^{-1}. We fix the velocity of the low-velocity component to be 20 km s^{-1} and include it in fits of all lines except the weak $J = (24–23)$ transition. The measured line properties of each transition of HC$_3$N and H^{13}CCCN from these fits are given in Table 2.

By comparing the HC$_3$N and H^{13}CCCN line brightness temperatures, we can estimate the optical depth of the $J = (3–2)$ and (5–4) lines, by assuming the [^{12}C/^{13}C] ratio in the Galactic center to be 25 (Wilson & Rood 1994; Riquelme et al. 2010). For each cloud, we then measure the ratio of the fluxes of the two transitions of HC$_3$N and H^{13}CCCN, averaging together the values for multiple Gaussian components, if present. Using the $J = 3–2$ ($J = 5–4$) transitions, we subsequently find HC$_3$N-to-H^{13}CCCN line ratios of 26 ± 2 (22 ± 2) for GCM 0.25+0.01, 21 ± 1 (20 ± 1) for GCM −0.02–0.07, and 33 ± 6 (25 ± 7) for GCM −0.13–0.08. In all cases, the ratio derived from the $J = (5–4)$ line is slightly smaller than that from the $J = (3–2)$ line, consistent with the (5–4) line being somewhat less optically thin (as it is closer to the peak of the spectral line energy distribution; Walmsley et al. 1986). Overall, however, all of these values are consistent with the main HC$_3$N transitions being optically thin, with $\tau \lesssim 0.5$. While this may not be a good assumption in the highest column density source Sgr B2, this assumption should largely hold for the rest of the CMZ.
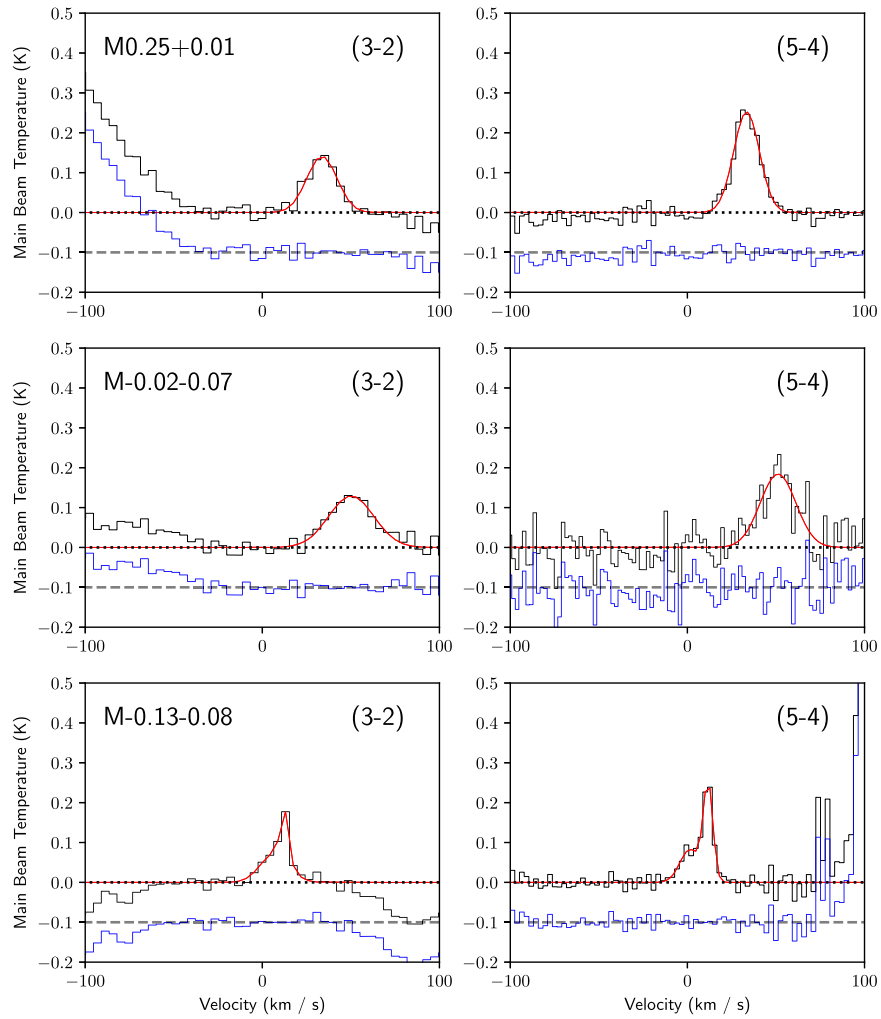
3.1. Ratio Maps

Using the Mopra maps of the (3–2), (5–4), and (10–9) lines of HC$_3$N, we then construct maps of ratios between these lines across the entire CMZ (the (24–23) map is not used because this transition is only detected in a few isolated positions beyond the three clouds already probed). The resulting ratio maps are shown in Figure 4.

Before attempting to identify trends, it should be noted that the Sgr B2 core at $l \sim 0.65$ degrees exhibits unresolved absorption against its numerous H II regions in the $J = (3–2)$ line and to a slightly lesser extent in the $J = (5–4)$ line, causing an apparent peak in the ratio maps that is not due to differing excitation in this source. Ignoring this area, we see that the (5–4)/(3–2) line ratio does not change greatly over the CMZ. The largest median (5–4)/(3–2) ratios, 0.74 ± 0.09, are found in the Sgr A complex between $l = −0°.2$ and $l = +0°.2$ and including the GCM −0.02–0.07 and GCM −0.13–0.08 clouds. The ratio is slightly smaller (0.61 ± 0.09) in the gas between $l = +0°.2$ and $l = 0.6$ degrees, which includes GCM 0.25 +0.01, the "dust ridge" (Lis et al. 1994; Immer et al. 2012), and the gas around Sgr B2. Finally, the smallest ratio, 0.52 ± 0.06, is found in the gas at $l > 1°.5$. This trend is slightly modified when we examine the map of the ratio of the $J = (10–9)$ to $J = (3–2)$ lines, which are more widely spaced in excitation energy. Here, gas in the outer CMZ at $l > 1°$ has a smaller median (10–9)/(3–2) ratio of 0.18 ± 0.04, compared to a median ratio of 0.33 ± 0.11 in gas with $|l| < 1°$.

As we find that the brightest lines, $J = (3–2)$ and (5–4), are optically thin in clouds representative of the gas outside of the Sgr B2 core (and the weaker, higher-J lines should follow suit), these trends should not be driven by differences in line opacity. Rather, they are indicative of changes in temperature, density, and/or the relative abundance of low-excitation and high-excitation HC$_3$N. In particular, the observed distribution of the HC$_3$N (10–9)/(3–2) ratio shows that there is more high-excitation gas in the inner $R = 1°/140$ pc. As a systematic temperature difference is not seen between the inner and outer CMZ gas (Ginsburg et al. 2016; Krieger et al. 2017), this is more likely to be a density effect. The inner CMZ gas would then have a higher average gas density, either because clouds in the inner CMZ have a larger fraction of gas in a high-density
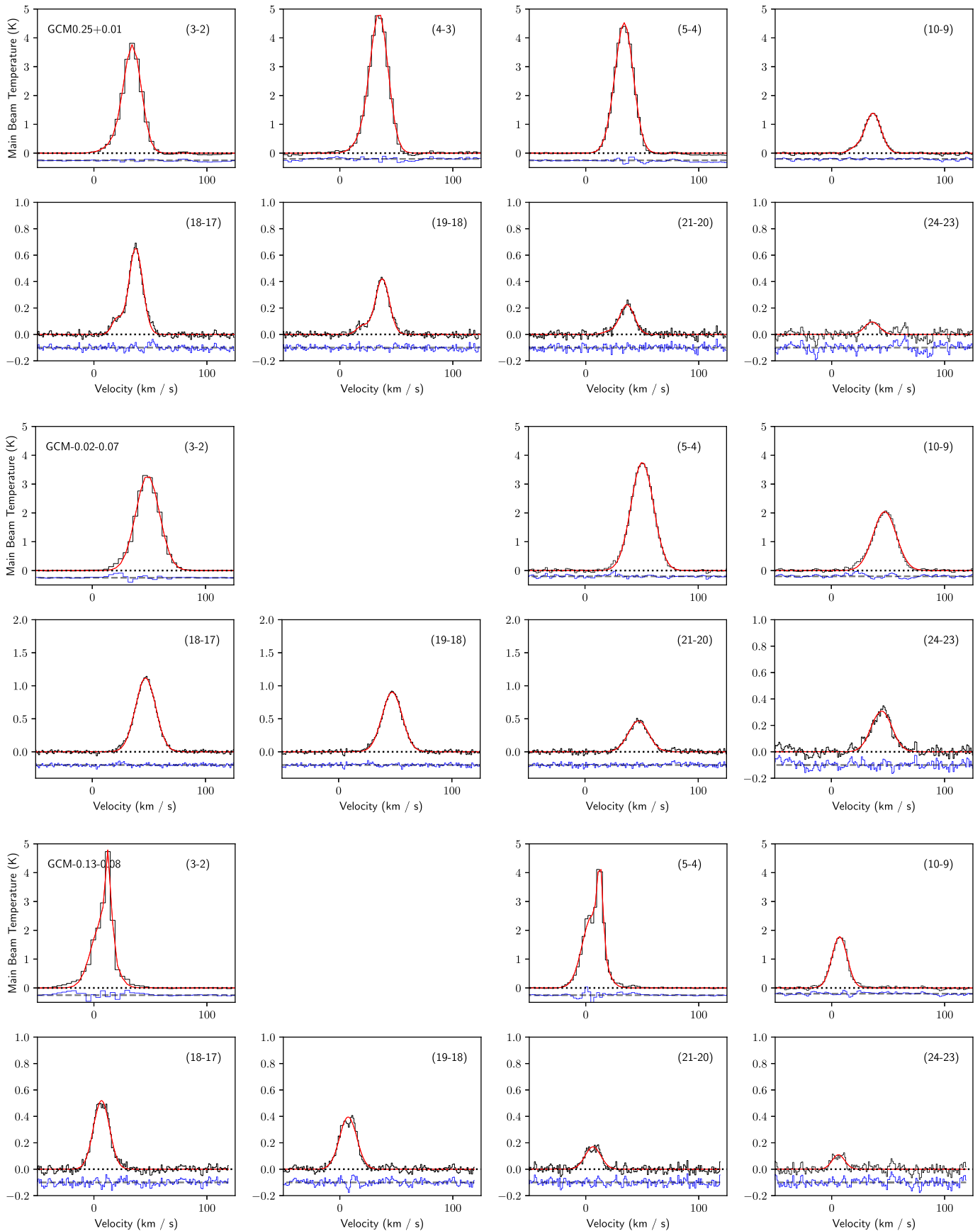
Figure 2. Spectra of HC$_3$N in the GCM 0.25+0.01 cloud (top), the GCM –0.02–0.07 cloud (middle), and the GCM –0.13–0.08 cloud (bottom). Gaussian fits to each line are overplotted in red, and the residuals of the fits are plotted below the spectrum in blue.

Figure 3. Spectra of H^{13}CCCN in the GCM 0.25+0.01 cloud (top), the GCM −0.02–0.07 cloud (middle), and the GCM −0.13–0.08 cloud (bottom).
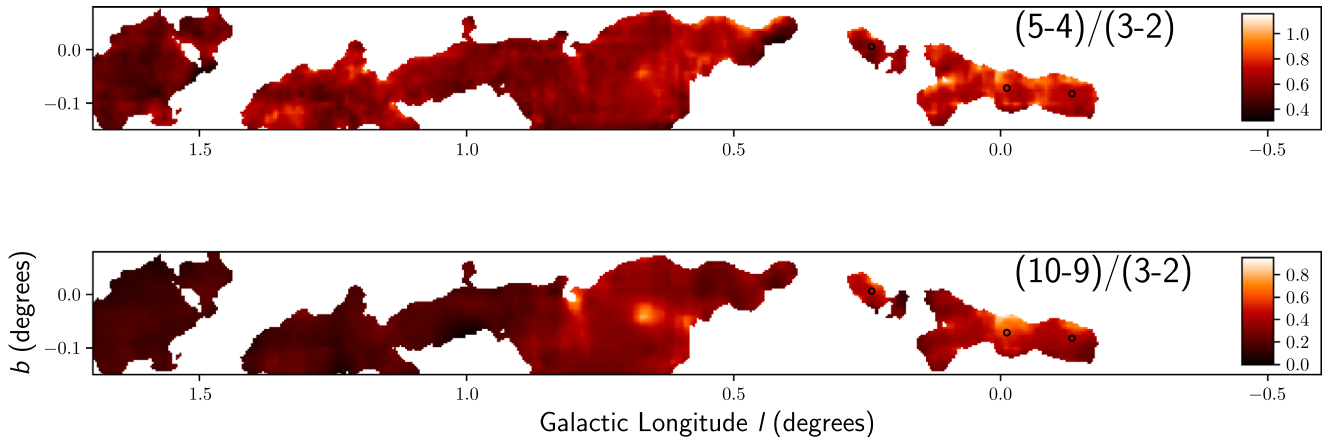
Figure 4. Ratio maps of the HC$_3$N J = (5–4) to (3–2) lines (top) and J = (10–9) to (3–2) lines (bottom). As in Figure 1, circles indicate the positions of pointed observations made with the GBT. A qualitative difference between the inner CMZ (right half) and the 100 pc < r < 200 pc region (left half) is evident: the excitation is lower beyond the orbit of Sgr B2. This difference suggests that the gas in the outer CMZ has a lower average density and/or lacks a high-density (high-excitation) component, consistent with models in which the CMZ is fed by highly turbulent, non-star-forming gas driven in by the Galactic bar.

gas component than those in the outer CMZ, or because the gas in the inner CMZ attains higher peak densities than that in the outer CMZ. We discuss the possibility that this result could also be affected by the relative abundances in Section 4.1.

To better understand the quantitative constraints on the physical conditions of the gas from these maps, we next turn to non-LTE modeling of the HC$_3$N lines. Given the relatively low J numbers of the mapped transitions, excitation modeling of

Table 2
Measured Line Parameters

| Source	Species	Transition	Resolution	v_{cen} (km s^{-1})	v_{fwhm} (km s^{-1})	Peak T_{MB} (K)	$\int T_{MB} dv$ (km s^{-1})
GCM 0.25–0.01 (a)	H^{13}CCCN	(3–2)	28	33.7 ± 0.6	20.1 ± 1.5	0.14 ± 0.01	3.0 ± 0.2
		(5–4)	17	33.4 ± 0.3	17.2 ± 0.8	0.25 ± 0.01	4.6 ± 0.1
	HC$_3$N	(3–2)	28	34.3 ± 0.1	18.4 ± 0.1	3.65 ± 0.01	71.3 ± 0.1
		(4–3)	21	34.8 ± 0.1	18.7 ± 0.1	4.80 ± 0.02	95.3 ± 0.1
		(5–4)	17	34.0 ± 0.1	19.0 ± 0.1	4.52 ± 0.01	91.5 ± 0.1
		(10–9)	40	36.5 ± 0.1	16.7 ± 0.2	1.39 ± 0.01	24.7 ± 0.1
		(18–17)	40	37.0 ± 0.1	14.5 ± 0.1	0.65 ± 0.01	10.1 ± 0.1
		(19–18)	40	37.6 ± 0.1	14.6 ± 0.3	0.42 ± 0.01	6.5 ± 0.1
		(21–20)	40	36.6 ± 0.2	15.2 ± 0.6	0.22 ± 0.01	3.6 ± 0.1
		(24–23)	40	35.7 ± 0.7	15.1 ± 1.7	0.09 ± 0.01	1.5 ± 0.2
GCM 0.25–0.01 (b)	HC$_3$N	(3–2)	28	20.0	23.0 ± 0.8	0.33 ± 0.01	8.1 ± 0.4
		(4–3)	21	20.0	18.9 ± 1.3	0.38 ± 0.03	7.7 ± 0.8
		(5–4)	17	20.0	14.5 ± 1.1	0.13 ± 0.01	2.0 ± 0.3
		(10–9)	40	20.0	12.1 ± 2.0	0.14 ± 0.02	1.8 ± 0.4
		(18–17)	40	20.0	10.2 ± 0.7	0.11 ± 0.01	1.2 ± 0.1
		(19–18)	40	20.0	12.0 ± 1.6	0.06 ± 0.01	0.8 ± 0.1
		(21–20)	40	20.0	11.6 ± 5.8	0.02 ± 0.01	0.2 ± 0.2
GCM –0.13–0.08 (a)	H^{13}CCCN	(3–2)	28	7.0 ± 0.1	19.0 ± 2.9	0.07 ± 0.01	1.5 ± 0.3
		(5–4)	17	1.5 ± 1.3	13.3 ± 2.9	0.08 ± 0.01	1.2 ± 0.3
	HC$_3$N	(3–2)	28	7.0 ± 0.1	22.0 ± 0.4	2.29 ± 0.04	53.7 ± 0.2
		(5–4)	17	5.7 ± 0.1	20.6 ± 0.1	2.50 ± 0.01	54.6 ± 0.1
		(10–9)	40	7.0 ± 0.1	15.9 ± 0.2	1.78 ± 0.02	30.1 ± 0.1
		(18–17)	40	6.7 ± 0.1	16.8 ± 0.3	0.52 ± 0.01	9.3 ± 0.1
		(19–18)	40	7.4 ± 0.1	18.0 ± 0.3	0.40 ± 0.01	7.6 ± 0.1
		(21–20)	40	6.4 ± 0.4	16.3 ± 1.0	0.17 ± 0.01	2.9 ± 0.1
		(24–23)	40	6.0 ± 0.6	13.0 ± 1.5	0.11 ± 0.01	1.5 ± 0.2
GCM –0.13–0.08 (b)	H^{13}CCCN	(3–2)	28	12.5 ± 0.6	5.4 ± 0.9	0.13 ± 0.02	0.7 ± 0.2
		(5–4)	17	11.7 ± 0.2	6.3 ± 0.5	0.24 ± 0.02	1.6 ± 0.2
	HC$_3$N	(3–2)	28	12.7 ± 0.1	6.0 ± 0.1	2.87 ± 0.07	18.4 ± 0.4
		(5–4)	17	12.7 ± 0.1	5.7 ± 0.1	2.57 ± 0.01	15.5 ± 0.1
GCM –0.02–0.07	H^{13}CCCN	(3–2)	28	50.2 ± 0.8	30.0 ± 0.1	0.13 ± 0.01	4.1 ± 0.2
		(5–4)	40	51.2 ± 0.5	23.8 ± 1.2	0.18 ± 0.01	4.7 ± 0.3
	HC$_3$N	(3–2)	28	48.9 ± 0.1	24.6 ± 0.1	3.31 ± 0.01	86.6 ± 0.2
		(5–4)	40	50.6 ± 0.1	23.4 ± 0.1	3.75 ± 0.02	93.7 ± 0.8
		(10–9)	40	47.1 ± 0.1	24.3 ± 0.2	2.04 ± 0.01	52.8 ± 0.5
		(18–17)	40	47.1 ± 0.1	21.1 ± 0.1	1.12 ± 0.01	25.0 ± 0.2
		(19–18)	40	47.2 ± 0.1	20.8 ± 0.2	0.90 ± 0.01	20.0 ± 0.2
		(21–20)	40	47.1 ± 0.1	20.9 ± 0.4	0.47 ± 0.01	10.4 ± 0.2
		(24–23)	40	44.4 ± 0.3	21.4 ± 0.7	0.31 ± 0.01	7.0 ± 0.3

just these three lines is unable to robustly constrain the full physical conditions of the gas in this region. However, as we have three clouds for which we have observed additional high-J HC$_3$N lines, we attempt to gain some insight into the global gas densities in the CMZ by modeling HC$_3$N excitation in these clouds.

3.2. Excitation Modeling

We use the publicly available statistical equilibrium radiative transfer code RADEX (van der Tak et al. 2007), a zero-dimensional non-LTE code employing escape probability formalism to model the observed line intensities as a function of the physical conditions. The escape probability method simplifies the radiative transfer calculation by assuming that photons either completely escape the source (the likelihood of this is dependent on the local opacity) or are immediately absorbed at the same location where they were emitted. The radiative coefficients for the observed rotational transitions of HC$_3$N are taken from the Cologne Database for Molecular Spectroscopy (Müller et al. 2005), and the collisional coefficients are taken from Faure et al. (2016). Two collisional partners, ortho-H$_2$ and para-H$_2$, are considered, and we adopt a statistical ortho-to-para ratio for H$_2$ (3:1); however, varying this does not appear to have a strong effect on the results.

RADEX takes as input parameters the kinetic temperature, the number density of H$_2$, the column density of HC$_3$N per velocity element, and the line FWHM (these last two values are used by RADEX to determine the local opacity). Additionally, a background radiation temperature is specified; this value is held fixed for all of the fitting we conduct. We adopt a representative FWHM value for each individual cloud: 16 km s^{-1} for GCM 0.25+0.01, 22 km s^{-1} for GCM − 0.02–0.07, and 28 km s^{-1} for GCM − 0.13–0.08. We fit a two-component model of temperature and density for all three clouds. We consider kinetic temperatures between 20 and 300 K for both
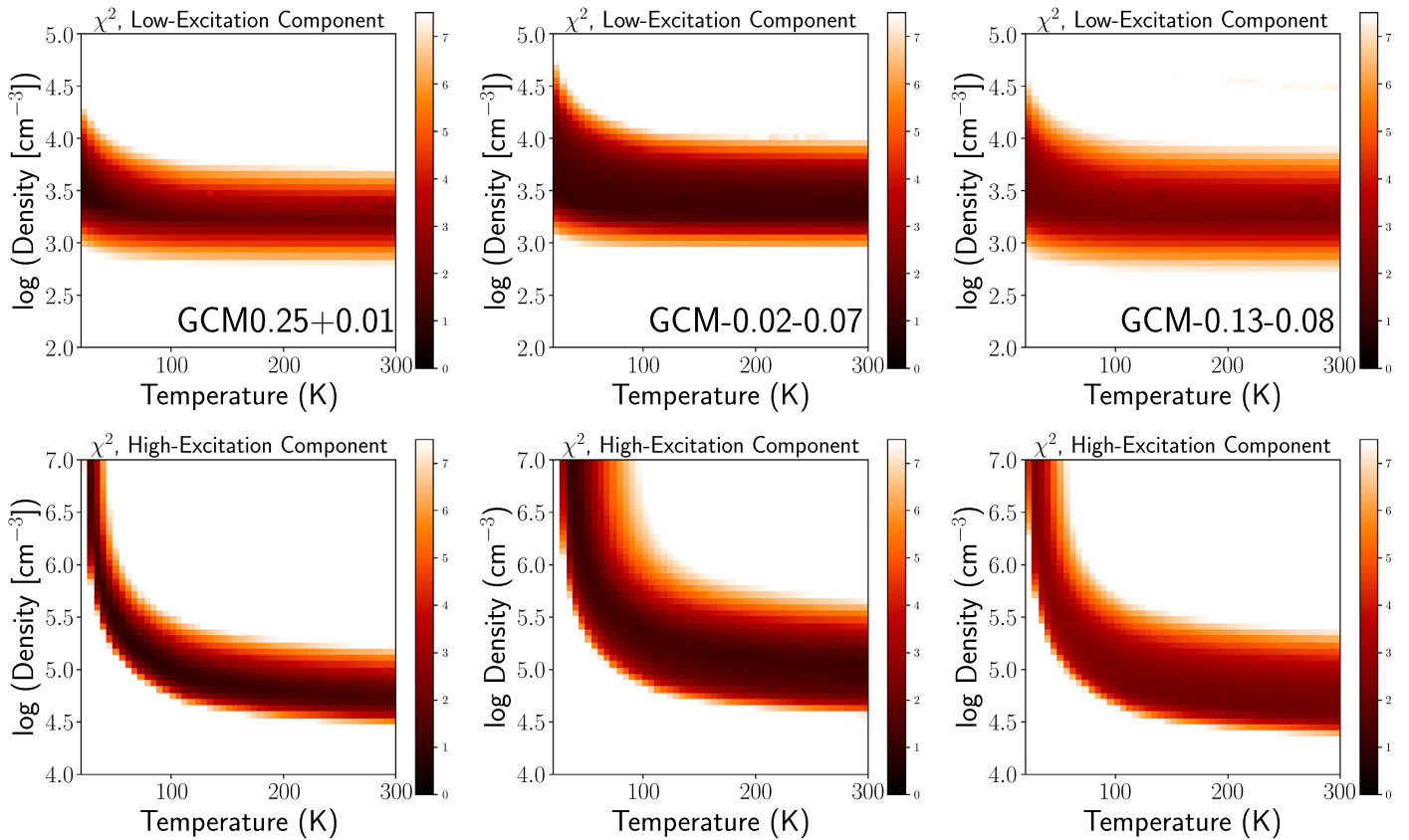
Figure 5. Chi-squared values from fitting computed grids of density and temperature values from a two-component RADEX fit to the flux of the observed HC$_3$N lines. Fits are shown separately for GCM 0.25+0.01 (left), GCM –0.02–0.07 (middle), and GCM –0.13–0.08 (right). Top row: temperature and density constraints on the low-excitation component. Bottom row: temperature and density constraints on the high-excitation component.

excitation components. For the low-excitation component, we consider H$_2$ number densities between 10^2 and 10^5 cm^{-3} and HC$_3$N column densities between 10^{14} and 10^{16} cm^{-2}. For the high-excitation component, we consider H$_2$ number densities between 10^4 and 10^7 cm^{-3} and HC$_3$N column densities between 10^{13} and 10^{15} cm^{-2}.

Using RADEX, we then compute line intensities for the three fixed FWHM values and a range of temperatures, densities, and column densities. We evaluate the line intensities over a 30 × 30 grid of input temperatures (linearly spaced) and densities (logarithmically spaced), with a separate grid computed for each of 20 logarithmically spaced values of the column density. This procedure is repeated for both the low-excitation and high-excitation components, to make two separate sets of output line intensities. In addition to reporting the brightness temperature and flux for all transitions of HC$_3$N between $J = (1–0)$ and $J = (24–23)$, RADEX also reports the line opacity, which we use to verify that the modeled (3–2) and (5–4) lines are optically thin, consistent with our observations.

To conduct a two-component fit, we then perform chi-squared fitting of the observed line fluxes (the sum of the one or two Gaussian components fit to each line) to the summed model fluxes from each combination of values in the low-excitation and high-excitation RADEX runs. The results of this fitting are displayed in Figures 5–7. Figure 5 shows the chi-squared values for fitting to each cloud as 2D grids of temperature and density, marginalized over all values of the column density. Separate grids are shown for the low- and high-excitation components. Figure 6 shows chi-squared values from fits to each cloud as 1D plots for the density, marginalized over all values of temperature and

column density. The values for the low- and high-excitation components are shown separately. Figure 7 shows the chi-squared values from fits to each cloud as 1D plots for the column density, marginalized over all values of temperature and density. Again, the values for the low- and high-excitation components are shown separately.

In combination with the chi-squared fitting we have applied an additional joint constraint on the abundance and path length of the low-excitation component. If the gas traced by low-excitation lines of HC$_3$N is truly tenuous, it could have a path length up to the entire depth of the CMZ (e.g., ∼100 pc; Kruijssen et al. 2015). However, in this case, it should trace gas with a wide range of velocities (e.g., Figure 4 of Kruijssen et al. 2015, in which velocities along a single line of sight should span ∼100 km s^{-1}), and so the relatively narrow line widths of 15–20 km s^{-1} that are observed should rule this out. We adopt a maximum path length of 10 pc, which is a conservative assumption that would still mean that the clouds are more extended along the line of sight than they appear in the plane of the sky.

To determine a reasonable maximum HC$_3$N abundance for the low-excitation gas in the CMZ, we first determine the mean HC$_3$N abundance for our best-fit model parameters. We compare the total HC$_3$N column density from both the low- and high-excitation gas to an estimate of the total H$_2$ column in each cloud from *Herschel*-HiGal observations of the Galactic center (Battersby et al. 2011, 2018, in preparation; Molinari et al. 2011). Note that it is not possible to separately estimate the abundances of the individual excitation components, as the fraction of the H$_2$ column associated with each component is
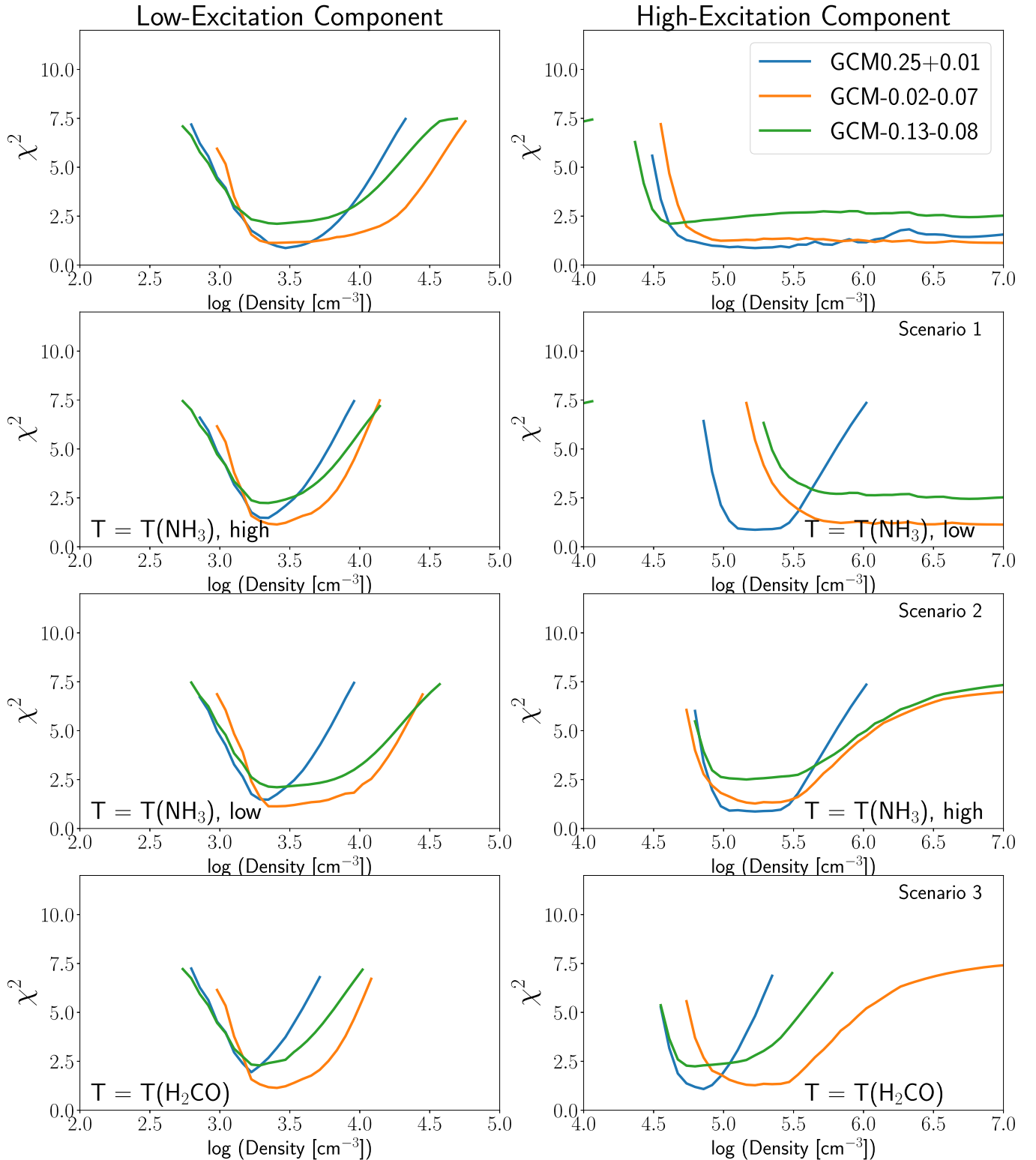
Figure 6. Chi-squared values from RADEX fitting for the density of the low- and high-excitation components for each of the three observed clouds, GCM 0.25+0.01, GCM –0.02–0.07, and GCM –0.13–0.08, marginalized over all other parameters. Top row: no constraint on the kinetic temperature is applied. Second row: scenario 1 from Section 4: the temperature of the low- and high-density component is restricted to be within ∼20% of the low and high kinetic temperature component, respectively, as measured from NH₃ lines at the source position by Krieger et al. (2017). Third row: scenario 2 from Section 4: the temperature of the low- and high-density component is restricted to be within ∼20% of the high and low kinetic temperature component, respectively, as measured from NH₃ lines at the source position by Krieger et al. (2017). Bottom row: scenario 3 from Section 4: the temperature of both components is restricted to be within ∼20% of the kinetic temperature measured from H₂CO lines at the source position by Ginsburg et al. (2016).
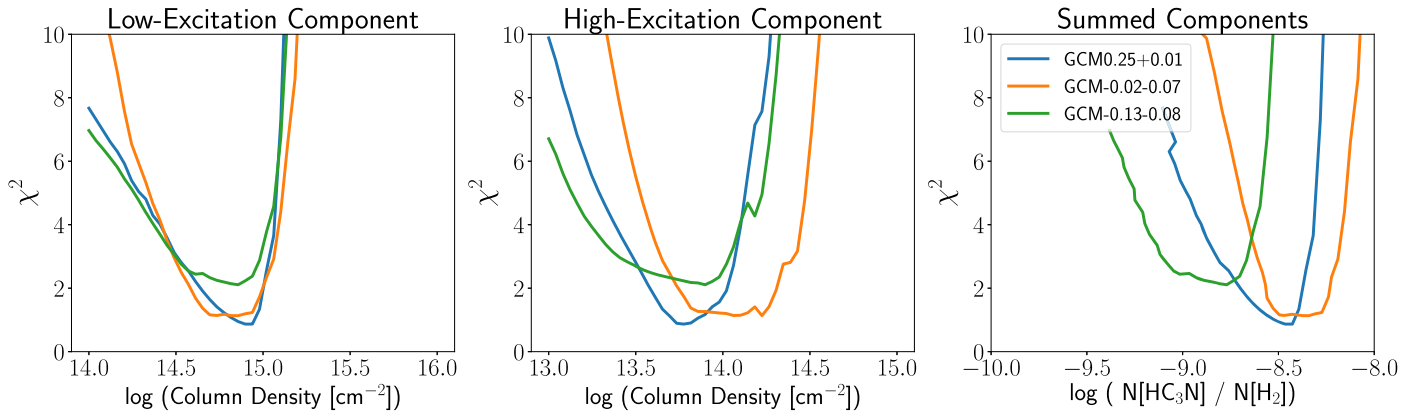
Figure 7. Chi-squared values for the column density of the low- and high-excitation components (left and middle) for each of the three observed clouds, GCM 0.25 +0.01, GCM –0.02–0.07, and GCM –0.13–0.08, marginalized over all other parameters. On the right, we show the best-fit abundance from summing the best-fit column densities and comparing to the average *Herschel*-derived H_2 column densities extracted from the same apertures as the HC_3N spectra.

unknown. The resulting best-fit mean abundances are shown in the right panel of Figure 7 and are in the range of $(2–5) \times 10^{-9}$, consistent with prior estimates for Galactic center clouds ranging between 10^{-11} and 5×10^{-9} for Galactic center clouds (Morris et al. 1976; de Vicente et al. 2000). While de Vicente et al. (2000) suggest that HC_3N abundances in several of the Sgr B2 hot cores could be as high as 10^{-7}, for the extended clouds studied here we adopt a maximum value for the HC_3N abundance in the low-excitation component of 10^{-8}, consistent with the most extreme values measured in the nuclei of other galaxies (Mauersberger et al. 1990; Meier & Turner 2005; Aalto et al. 2007). We can then define a column density threshold as a function of the gas volume density:

$$N_{max} = l * n * N[HC_3N]/N[H_2], \qquad (1)$$

where l is the maximum path length in cm, N_{max} is the maximum allowed column density, n is the modeled volume density, and $N[HC_3N]/N[H_2]$ is the maximum allowed HC_3N abundance. Eliminating those RADEX solutions that would require unphysically large path lengths or abundances sets both the lower bound on the gas densities of the low-excitation component shown in Figure 5 and the upper bound on the column densities for the low-excitation component shown in Figure 7.

Overall, as expected, the temperature of these three clouds is not constrained by our fits to the HC_3N line intensities. The density of the low-excitation gas is constrained to be between 10^3 and 10^4 cm^{-3} with no significant difference in this value between the three clouds. The density of the high-excitation gas is constrained to be larger than 3×10^4 cm^{-3} for all three clouds. If we assume that the gas is warmer than 50 K, as several previous studies have indicated, then the upper bound on this density is between 3×10^5 and 10^6 cm^{-3}; without a constraint on the temperature, densities up to 10^7 cm^{-3} are allowed. The column density of the low-excitation gas is constrained to be between $\sim 3 \times 10^{14}$ and 10^{15} cm^{-3} for all three clouds. That of the high-excitation gas is constrained to be between $\sim 3 \times 10^{13}$ and 3×10^{14} cm^{-3}, with somewhat higher values favored for GCM –0.02–0.07 than for the other two clouds. We find that the density of the low-excitation component is $<10^{4.5}$ cm^{-3} for all temperatures considered. The density of the high-excitation component is $>10^{4.5}$ cm^{-3}, again for all clouds and temperatures considered.

Comparing the best-fit column densities of the low- and high-excitation components, we find that the fraction of the HC_3N column coming from gas with $n > 10^4$ cm^{-3} is $\sim 15\%$ in all three clouds. From the range of allowed column densities for each source, there is a suggestion that this fraction may be slightly lower in GCM 0.25+0.01 than in GCM –0.13–0.08 and GCM –0.02–0.07; however, the uncertainties are too large to make a convincing claim.

4. Discussion

4.1. The HC_3N Abundance and Its Implications

In the three individual Galactic center clouds studied here, we infer HC_3N abundances in the range of $(2–5) \times 10^{-9}$ (a factor of 2.5 variation between the three clouds). This is comparable to HC_3N abundances measured in the nuclei of NGC 253 (4×10^{-9}; Mauersberger et al. 1990) and IC 342 (6×10^{-10}–3×10^{-9}; Meier & Turner 2005). It is also similar to the HC_3N abundance in the Orion hot core (2×10^{-9}; Blake et al. 1987). This is not unexpected given the chemical similarity of the bulk CMZ gas to hot cores elsewhere in the Galaxy (Requena-Torres et al. 2006). However, because the abundances we measure are referenced to H_2 column densities from *Herschel* dust continuum observations, they apply only to the sum of the two observed excitation components. That we do not constrain the relative abundance of the two components is a source of uncertainty in our analysis and for interpreting results on the dense gas fraction in the three main clouds and overall in the CMZ.

Chemical models predict a certain amount of abundance variation for HC_3N. Current chemical models for molecular clouds favor the gas-phase formation of HC_3N via a neutral–neutral reaction (Fukuzawa et al. 1998; Araki et al. 2016; Hily-Blant et al. 2018):

$$CN + C_2H_2 \rightarrow HC_3N + H. \qquad (2)$$

While many chemical models of HC_3N consider its formation in dark clouds (e.g., to reproduce the abundances of the cyanopolyyne peak in the Taurus Molecular Cloud; Suzuki et al. 1992), where cold core chemistry efficiently produces both the parent species C_2H_2 and HC_3N, such conditions do not match what is seen in the CMZ. However, HC_3N is also produced easily in a hot core environment like that seen globally in the CMZ, provided that its parent species C_2H_2 is liberated from grains (as has been observed in hot

cores; Lahuis & van Dishoeck 2000) since C_2H_2 is not efficiently produced in the gas phase under these conditions (Brown et al. 1988; Charnley et al. 1992).

In a time-dependent chemical model of a hot core at a fixed temperature and density, there is a nearly 3 order of magnitude difference between the peak HC_3N abundance (reached in a few $\times 10^4$ yr) and the steady-state abundance reached in $\sim 10^6$ yr (Chapman et al. 2009). As the formation reaction for HC_3N has a weak temperature dependence, variations in temperature are expected to have only a small impact on its abundance. This is consistent with what is seen in the Chapman et al. (2009) models, where changing the temperature from 200 to 100 K results in column density changes of less than 0.5 dex, while increasing the density by an order of magnitude correspondingly increases the HC_3N column density by an order of magnitude.

4.1.1. The Absolute Dense Gas Fraction in Individual Clouds

If we assume that the fractional HC_3N abundance is the same in the two excitation components that we observe, then we can interpret the fraction of the HC_3N column coming from gas with $n > 10^4$ cm^{-3} ($\sim 15\%$) as the actual fraction of dense molecular gas in these clouds. However, we cannot rule out that these components actually have different abundances, as we do not have a direct constraint on the abundances of the individual components. If we allow the relative abundances of the two components to vary by an amount equal to the variation in the total HC_3N abundance seen between the different clouds in this analysis (a factor of 2.5), then the typical dense gas fraction would be loosely constrained to be between 6% and 37%. Interestingly, Morris et al. (1976) in a two-component model of HC_3N in Sgr B2 found that the denser "core" component had a lower HC_3N abundance than the lower-density "halo" component, which, if it applied more globally, would result in a larger value for the dense gas fraction. A more precise estimate will ultimately require comparison of the HC_3N results with those of CO or another proxy gas tracer, in order to infer the abundance relative to H_2 for each component.

4.1.2. The Relative Dense Gas Fraction across the CMZ

We see a difference in the ratio of the HC_3N (10–9) line (which primarily traces the high-excitation HC_3N component) and (3–2) line (which primarily traces the low-excitation HC_3N component) in the CMZ for gas between $|l| < 1°$ and gas at $l > 1°$. If the relative HC_3N abundance of these two excitation components (whether or not they are identical) does not change, then we argue in Section 3.1 that the different (10–9)/(3–2) line ratios are likely to be due to a difference in the gas density of the two components. However, if these components represent physically and chemically distinct gas, it is also possible that a change in the relative HC_3N abundances in the low- and high-excitation components could reproduce this line ratio signature. These abundance differences would be unlikely to be driven by temperature; as has been previously noted, the inner CMZ gas is not systematically warmer (or colder) than the gas at $l > 1°$ (Ginsburg et al. 2016; Krieger et al. 2017). Similarly, Figure 2 of Mills & Battersby (2017) suggests that a change in abundance is also not likely to be an outcome of an enhanced shock chemistry in the inner regions, as shock-tracing molecules like HNCO and SiO still show elevated emission compared to the total H_2 column at $l > 1°$. So, while

we cannot rule out that a change in the relative HC_3N abundance of the components leads to a larger (10–9)/(3–2) ratio in gas with $|l| < 1°$, there is also no obvious reason to expect that the abundance of the high- or low-excitation component would change significantly at this radius.

4.2. The Degeneracy between Density and Temperature

The radiative transfer modeling of HC_3N excitation in Galactic center clouds yields no constraint on the gas temperature. This leads to a range of best-fitting solutions in which a solution for high densities and low temperatures appears equally likely as a solution for low densities and high temperatures for the range of lines modeled here. Due to this degeneracy between temperature and density, we assess three possible scenarios for the combination of temperature and density in each component. The impact of the temperature assumption for each of these scenarios is illustrated in Figure 6, and the ranges of temperatures and densities for each scenario are reported in Table 3.

4.2.1. Scenario 1: The High-excitation Component Is Cold

From our RADEX fits, densities up to 10^7 cm^{-3} (the upper bound on the density considered by our modeling) are allowed for the high-excitation component. Such high densities can only occur if the temperature of this component is quite low, $\lesssim 50$ K. However, NH_3 temperature studies of CMZ gas indicate that a significant fraction (50%–75%) of the CMZ gas traced by this molecule is at temperatures greater than 50 K (Hüttemeister et al. 1993; Krieger et al. 2017), much larger than the 15% of gas that we associate with the high-excitation component. Thus, to match the NH_3 observations, we would have to assume that part of the low-excitation component has $T < 50$ K and part has $T > 50$ K. Further, at the position we observe in GCM 0.25+0.01 the "low" kinetic temperature measured with NH_3 is 60 K, which would rule out gas with densities $>10^6$ cm^{-3}, at least in the southern part of this cloud.

H_2CO studies have the opposite problem: here, all of the dense CMZ gas is consistent with having temperatures >65 K, with no possibility of a substantial quantity of gas existing in a colder component (Ao et al. 2013; Ginsburg et al. 2016). Although cold, dense gas is not seen with H_2CO, modeling of thermal gas properties in the CMZ environment does predict that gas at densities approaching 10^7 cm^{-3} should, in the absence of internal heating sources like embedded protostars, begin to thermalize with dust temperatures that are ~ 20–30 K in the CMZ (Molinari et al. 2011; Clark et al. 2013). Thus, while current observational evidence does not favor this scenario, it is theoretically plausible. Qualitatively, this scenario would be consistent with both cosmic-ray and photodissociation region (PDR) heating, in which UV radiation and cosmic rays can more effectively penetrate and heat the low-density gas.

4.2.2. Scenario 2: The High-excitation Component Is Hot

In the reverse of the previous scenario, here the high-excitation/high-density component would be hot, while the low-excitation/low-density component would be cold. This is the scenario that best matches the two-temperature model of CMZ gas from NH_3 observations: the proportion of gas we find in the high/low-excitation components (15%/85%) is roughly consistent with that found by Krieger et al. (2017), with 20%–50%

Table 3
Adopted and Modeled Source Properties

	Excitation Component	GCM 0.25+0.01	GCM −0.02–0.07	GCM −0.13–0.08
$\log[N_{HC_3N}(\mathrm{cm}^{-2})]$	Low	$14.9^{+0.2}_{-0.5}$	$14.9^{+0.2}_{-0.5}$	$14.9^{+0.1}_{-0.5}$
$\log[N_{HC_3N}(\mathrm{cm}^{-2})]$	High	$13.8^{+0.3}_{-0.4}$	$14.2^{+0.1}_{-0.5}$	$13.9^{+0.1}_{-0.5}$
$N_{HC_3N(High)}/N_{HC_3N\,(Low)}$		0.08 ± 0.06	0.20 ± 0.15	0.10 ± 0.09
$\log[N_{H2}(\mathrm{cm}^{-2})]$[a]	Both	$22.40^{+0.07}_{-0.10}$	$22.28^{+0.04}_{-0.05}$	$22.67^{+0.08}_{-0.09}$
$\log[HC_3N/H_2]$	Both	$-8.5^{+0.2}_{-0.4}$	$-8.3^{+0.1}_{-0.3}$	$-8.8^{+0.2}_{-0.4}$
$T_{kin,NH3}$ (K)[b]	Low	64 ± 18	41 ± 8	26 ± 3
$T_{kin,NH3}$ (K)[c]	High	69 ± 4	102 ± 7	54 ± 6
$T_{kin,H2CO}$ (K)[d]	Both	140 ± 30	101 ± 13	91 ± 16
$\log[n_{H2}(\mathrm{cm}^{-3})]$	Low	$3.5^{+0.5}_{-0.4}$	$3.4^{+0.7}_{-0.2}$	$3.4^{+0.7}_{-0.3}$
$\log[n_{H2}(\mathrm{cm}^{-3})]$	High	>4.6	>4.7	>4.5
$\log[n_{H2}(\mathrm{cm}^{-3})]$[e]	Low	$3.3^{+0.3}_{-0.1}$	$3.4^{+0.3}_{-0.2}$	$3.3^{+0.5}_{-0.2}$
$\log[n_{H2}(\mathrm{cm}^{-3})]$[f]	High	$5.2^{+0.3}_{-0.2}$	>5.6	>5.5
$\log[n_{H2}(\mathrm{cm}^{-3})]$[g]	Low	$3.3^{+0.3}_{-0.1}$	$3.4^{+0.6}_{-0.1}$	$3.4^{+0.6}_{-0.2}$
$\log[n_{H2}(\mathrm{cm}^{-3})]$[h]	High	$5.2^{+0.3}_{-0.3}$	$5.2^{+0.5}_{-0.3}$	$5.2^{+0.5}_{-0.3}$
$\log[n_{H2}(\mathrm{cm}^{-3})]$[i]	Low	$3.2^{+0.3}_{-0.2}$	$3.4^{+0.3}_{-0.2}$	$3.3^{+0.4}_{-0.2}$
$\log[n_{H2}(\mathrm{cm}^{-3})]$[i]	High	$4.9^{+0.1}_{-0.2}$	$5.2^{+0.4}_{-0.3}$	$4.8^{+0.5}_{-0.1}$

Notes.
[a] From C. Battersby et al. (2018, in preparation) derived using *Herschel* data using the method of Battersby et al. (2011).
[b] From Krieger et al. (2017), derived from the (1, 1)–(2, 2) lines of NH_3.
[c] From Krieger et al. (2017), derived from the mean of the temperatures between the (2, 2)–(4, 4), (3, 3)–(6, 6), and (4, 4)–(5, 5) lines of NH_3.
[d] From Ginsburg et al. (2016) derived from the 3_{21}–2_{20} and 3_{03}–2_{02} lines of H_2CO.
[e] Determined by restricting temperature to the mean value measured by Krieger et al. (2017) using the $J > 2$ NH_3 lines (Scenario 1).
[f] Determined by restricting temperature to the value measured by Krieger et al. (2017) using the (1, 1)–(2, 2) NH_3 lines (Scenario 1).
[g] Determined by restricting temperature to the value measured by Krieger et al. (2017) using the (1, 1)–(2, 2) NH_3 lines (Scenario 2).
[h] Determined by restricting temperature to the mean value measured by Krieger et al. (2017) using the $J > 2$ NH_3 lines (Scenario 2).
[i] Determined by restricting temperature to the mean value measured by Ginsburg et al. (2016) (Scenario 3).

of the gas at 25–50 K, versus 50%–80% of the gas at 60–100 K. In this scenario, the density of the low-excitation gas would be in the range of $(1–5) \times 10^3 \mathrm{cm}^{-3}$, and the density of the high-excitation gas would be between 3×10^4 and $3 \times 10^5 \mathrm{cm}^{-3}$. Note that we expect the "cold" gas component to still be much warmer than the dust temperature, as densities $<10^4 \mathrm{cm}^{-3}$ are insufficient to thermalize the gas with the dust, and thus we would favor the "cold" gas being closer to 50 K than to 25 K. Qualitatively, this scenario would be consistent with shocks as a heating mechanism, with shocks both compressing the gas to higher density and heating it. Scenario 2 could also be consistent with some fraction of the dense gas having an internal heating source like embedded protostars.

4.2.3. Scenario 3: All the Gas Is Hot (or Not)

In this scenario, the discrepancy between NH_3 and H_2CO temperatures is resolved by assuming that the H_2CO temperatures are correct and the NH_3 temperatures are systematically low, possibly due to an unaccounted-for population of the non-metastable NH_3 transitions that are detected in GCM −0.02–0.07 and GCM –0.13–0.08 (Mills & Morris 2013). The low-density component would have densities between 10^3 and 10^4 cm^{-3}, and the high-density component would have densities in the range of $(1–3) \times 10^5$ cm^{-3}. These values would, however, not be fully representative of typical CMZ gas, as the three clouds observed here are somewhat warmer ($T_{H2CO} = 90–140$ K) than generally observed in the CMZ ($T_{H2CO} = 65$ K). The relatively low densities and high temperatures would be consistent with expectations that the

gas should not be well thermalized with the dust at densities $\lesssim 10^5$ cm^{-3} (Clark et al. 2013). We do not consider a scenario in which all of the gas is cold, as this is ruled out based on consistent findings of substantial columns of hot gas from both H_2CO and NH_3 (Ao et al. 2013; Mills & Morris 2013; Ginsburg et al. 2016; Krieger et al. 2017).

It is also possible that the gas density and temperature do not neatly co-vary, e.g., that there is both hot and cold high-density gas and hot and cold low-density gas. This might be expected if both cosmic rays and shocks/turbulent dissipation contribute to heating CMZ gas, and the relative strengths of these heating mechanisms vary across the CMZ. It could also occur if, e.g., some of the highest-density gas thermalizes with the dust and cools, while other clumps of high-density gas are internally heated by protostars, or if some of the low-density gas experiences additional PDR heating due to its proximity to H II regions in the CMZ.

4.2.4. Distinguishing between These Scenarios

While we favor Scenario 2, the current data do not allow us to robustly confirm this model. Conclusively determining the temperature of the HC_3N-emitting gas would make significant progress not just in constraining the density structure of CMZ gas but also in distinguishing between models for heating this gas. One of the best tools for making progress on this front will be interferometric observations of NH_3 and HC_3N with ALMA and the VLA, which should be able to isolate the clumpy gas. With both high spatial and spectral resolution, it will be easier to argue that NH_3 and HC_3N are tracing the same gas, and it

4.3. Comparison with Other Density Estimates

Prior to this work, there have been a number of studies conducting radiative transfer modeling of non-LTE gas conditions to match observed line intensities across the CMZ to the temperatures, volume densities, and column densities responsible for their excitation. Many of these studies have been conducted with the CO molecule. Dahmen et al. (1998) observe multiple isotopologues of CO (1–0) and fit the observed intensities and opacities to models with gas densities of $10^{3.0}$ cm^{-3} and temperatures of 50 K, which would apply to the bulk (most likely $\sim 2/3$ of the observed CMZ gas. Nagai et al. (2007) observe CO (3–2) and (1–0) and fit the observed intensities to models with gas densities of $10^{3.5-4.0}$ cm^{-3}, though they note that they are unable to find solutions to some regions that are affected by self-absorption. For comparison, Martin et al. (2004) performed excitation analyses of CO (7–6) and (4–3), which have higher excitation energies than the lines probed by Nagai et al. (2007) or Jones et al. (2013), and find densities in cloud interiors up to $10^{4.5}$ cm^{-3}, which is the upper limit to which their analysis code is sensitive. Typical CMZ gas densities in excess of 10^4 cm^{-3} have been supported by excitation analyses of H$_2$CO emission (Güsten & Henkel 1983; Zylka et al. 1992) and dense gas tracers like ^{13}CS, HCN, and HC$_3$N (Paglione et al. 1998; Jones et al. 2012, 2013).

CO has also been used to infer the presence of much lower density gas. Dahmen et al. (1998) estimate that one-third of the gas in the CMZ (and possibly up to two-thirds) is in a warm and tenuous component with densities of $10^{2.0}$ cm^{-3} and temperatures of 150 K. This component is also traced by H$_3^+$ (Oka et al. 2005) in the near-infrared and numerous hydrides observed with *Herschel* (Geballe & Oka 2010; Lis et al. 2010a, 2010b, 2012; Schilke et al. 2010; Menten et al. 2011; Monje et al. 2011; Sonnentrucker et al. 2013). Most of these species are observed in absorption toward multiple lines of sight against strong infrared and submillimeter continuum sources, especially toward Sgr B2 and Sgr A. The H$_3^+$ observations have characterized this gas component as warm ($T \sim 250$–350 K), diffuse ($n \sim 10$–100 cm^{-3}), and pervasive—the inferred sizes of the absorbing clouds are several tens of parsecs and are suggested to constitute a substantial fraction of the volume filling factor in the CMZ (Oka et al. 2005; Goto et al. 2008, 2011). However, as this component has thus far primarily been detected only in absorption toward pencil-beam lines of sight and in emission at extremely low spatial resolution from CO and CH (e.g., $9'$; Dahmen et al. 1998; Magnani et al. 2006; Riquelme et al. 2018), it is not clear whether it fills the entire CMZ or simply comprises the more extended envelopes of the known clouds, the bulk of which lie in a ~ 100 pc ring-like structure (Molinari et al. 2011; Kruijssen et al. 2015).

Locally higher densities have previously been inferred from analyses of individual clouds. Observations of multiple transitions of CS in several clouds (M –0.02–0.07, and the Sickle cloud, which abuts the Quintuplet star cluster) indicate that the highest gas densities in these clouds can range from a few $\times 10^5$ up to a few $\times 10^6$ cm^{-3} (Serabyn & Güsten 1991; Serabyn et al. 1992). Similar excitation analyses of multiple transitions of HC$_3$N show that even denser gas can be found in the Sgr B2 cloud, whose mean density is measured to be 10^5 cm^{-3} and the core of which has densities in excess of 10^7 cm^{-3} (Morris et al. 1976; Lis & Goldsmith 1991). Gas in the circumnuclear disk ~ 1–2 pc from the supermassive black hole Sgr A* is also measured to be extremely dense, with gas densities from CO and HCN reaching values up to 10^5–10^6 cm^{-3} (Requena-Torres et al. 2012; Mills et al. 2013; Smith & Wardle 2014).

Density estimates have also been made for two of the three clouds we focus on here. Observations of HC$_3$N (1–0) through (25–24) in GCM –0.02–0.07 were fit with two density components, with the lower-density component being several times 10^3 cm^{-3} and the high-density component being a few $\times$ 10^5 cm^{-3} (Walmsley et al. 1986). In GCM 0.25+0.01, densities are estimated to be comparable to the highest densities in GCM –0.02–0.07, lying between $\sim 8 \times 10^4$ cm^{-3} (Longmore et al. 2012) and a few $\times 10^5$ cm^{-3} (Kauffmann et al. 2013), though these estimates are based on a combination of column density and geometric arguments, and no excitation analysis of the density has been published. Notably, all of the global gas density studies (and the majority of density studies for individual clouds) have assumed a single density component.

By constraining two density components in the CMZ gas, we better quantify the distribution of CMZ gas densities that have typically been approximated as $n \sim 10^4$ cm^{-3} by fitting just a single density component and yielding an indeterminately weighted average of the true distribution of gas densities. We argue that, with $\sim 85\%$ of the HC$_3$N-detected gas having densities of $\sim 3 \times 10^3$ cm^{-3}, we should instead think of the "typical" gas density in the Galactic center clouds as being significantly less than 10^4 cm^{-3}. In fact, by focusing on the properties of gas near the center of three of the most massive, dense clouds in the CMZ, these results may in fact be biased toward measuring higher densities than are typically present in the CMZ. Future measurements of HC$_3$N lines away from the dense cloud centers would better show how representative these measured densities are. Finally, while we do not appear to directly probe the $n \sim 100$ cm^{-3} gas detected in some prior studies, our observations of densities from $\sim 10^3$ to 10^5 cm^{-3} suggest that there may be a continuum of gas densities that connects the observed clouds to this tenuous medium (perhaps consistent with the structure of cloud envelopes) rather than sharply defined "dense" clouds embedded in a pervasive, uniformly diffuse medium.

4.4. Dense Gas and Star Formation in the CMZ

Having analyzed the three clouds for which we observe the largest number of HC$_3$N lines, we return now to the ratio maps of HC$_3$N lines for the entire CMZ. Looking at the examples of best-fit models to the observed line intensities (Figure 8), we see that the ratio of the (10–9) line to the (3–2) line should be sensitive to the presence of gas at densities above 10^4 cm^{-3}, as line intensities from a $\sim 10^5$ cm^{-3} density component peak around $J = 12$, as can be seen in Figure 8. We then interpret regions of weaker (10, 9) emission as having a lower fraction of the $\gtrsim 10^4$ cm^{-3} density gas that is detected in all three of the clouds we observe.

As noted earlier, we see a transition in the (10–9)/(3–2) ratio in Figure 4, in which the (10–9) emission is relatively much weaker at $l > 1°$. We interpret this as there being a lower (or potentially negligible) fraction of $\gtrsim 10^4$ cm^{-3} density gas outside of a radius of ~ 140 pc. This is consistent with the
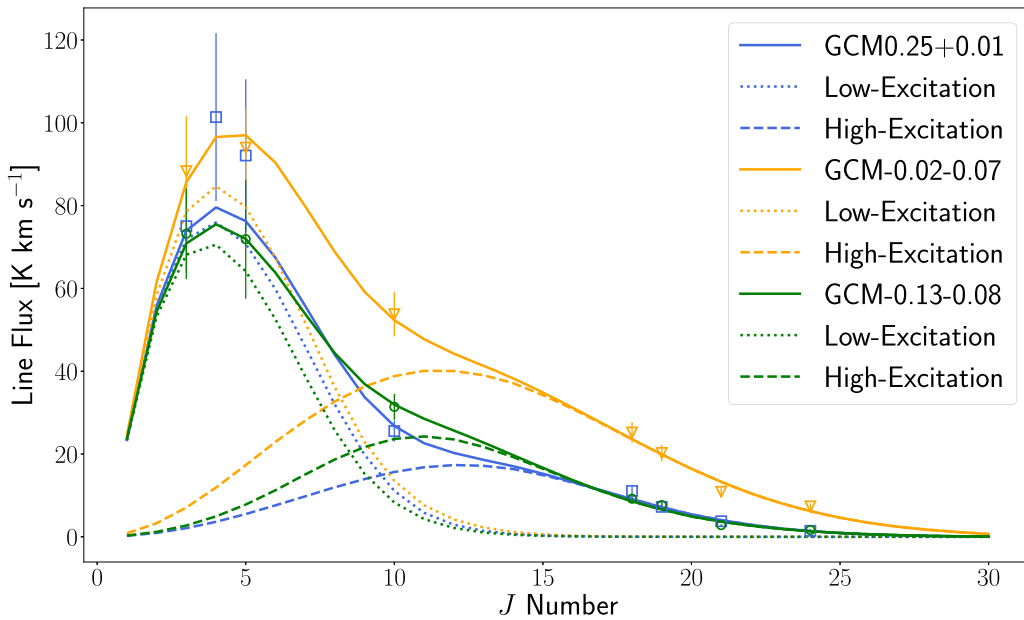
Figure 8. Comparison of the best fits from RADEX (solid line) to the total line flux (individual data points) of the observed HC₃N lines. Fits are shown for each of the three clouds: GCM 0.25+0.01, GCM –0.02–0.07, and GCM –0.13–0.08.

Krumholz et al. (2017) model that predicts that the gas density should sharply transition from values $\lesssim 10\,\mathrm{cm}^{-3}$ to having an average density of $\sim 10^4\,\mathrm{cm}^{-3}$ at this galactocentric radius (see, e.g., their Figure 13). This is consistent with their model, which says that this $\sim 100\,\mathrm{pc}$ radius is a minimum in the shear that transports gas inward and is a location where gas builds up and undergoes starbursts. With the existing maps, we can only test for this signature on the positive-longitude side of the CMZ; however, the Krumholz et al. (2017) model would predict that the same density transition occurs at negative longitudes beyond Sgr C as well.

If the high-excitation gas is much hotter than 50 K (as we argue is the more likely scenario), the three observed clouds would all have peak gas densities less than $4 \times 10^5\,\mathrm{cm}^{-3}$, much lower than found for the Sgr B2 cloud ($\sim 10^7\,\mathrm{cm}^{-3}$; Lis & Goldsmith 1991). If, however, the dense gas is at the lowest temperatures measured at these positions using NH₃, this could allow for gas densities in at least two of the observed clouds (GCM –0.02–0.07 and GCM –0.13–0.08) to reach values $> 10^6\,\mathrm{cm}^{-3}$, consistent with the volume density threshold for star formation of $\sim 10^6\,\mathrm{cm}^{-3}$ that is predicted by the Krumholz et al. (2017) model. Although GCM 0.25+0.01, GCM –0.02–0.07, and GCM –0.13–0.08 are not actively forming stars at the same rate as Sgr B2, all three clouds do at least have some signature of star formation (either water masers or compact H II regions; Goss et al. 1985; Ho et al. 1985; Lis et al. 1994; Lu et al. 2017). To have the densities in these clouds then be consistent with the Krumholz et al. (2017) threshold requires (1) that the high-density gas be at temperatures $T < 50$ K, (2) that high densities are only reached in a small fraction of the gas on spatial scales much smaller than those averaged together in this study, or (3) that the densities we measure toward these three positions are not representative of the (higher) densities found elsewhere in the cloud. In the future, stronger tests of the Krumholz et al. (2017) threshold for star formation can be made both by measuring gas densities on smaller spatial scales across entire clouds and by measuring densities toward

additional CMZ gas that is not associated with signatures of star formation.

In environments outside of the Galactic center, the amount of star formation in a cloud has also been linked to the fraction of gas that exists at higher (column) densities (e.g., Imara 2015). ALMA observations of GCM 0.25+0.01 have already shown evidence for an excess of high column density gas, deviating from a lognormal column density probability distribution function, which is associated with a star-forming core in this cloud (Rathborne et al. 2015). We might expect to find a similar excess of high volume density gas originating from star-forming structures in which self-gravity has overcome the turbulent pressure. Currently, the precision of our observations is insufficient to measure variations in the amount of high-density gas in the three observed clouds. However, we would predict a lower fraction of high-density ($n > 10^5\,\mathrm{cm}^{-3}$) gas in clouds with little to no star formation like GCM 0.25+0.01, compared to GCM –0.02–0.07 and GCM –0.13–0.08, and ultimately much less than in Sgr B2. Observations of a larger number of lines (particularly including the isotopologues of all transitions to constrain the opacity in each component) should enable these measurements in the future.

5. Conclusion

We have studied multiple transitions of HC₃N in the central $R \sim 300\,\mathrm{pc}$ or CMZ of our Galaxy. We analyzed both maps of HC₃N (3–2), (5–4), and (10–9) across the full CMZ and pointed observations of higher-J lines toward the GCM 0.25+0.01, GCM –0.02–0.07, and GCM –0.13–0.08 clouds. By conducting radiative transfer modeling of these lines using the RADEX code, we have arrived at the following results:

1. In all three clouds we find two density components, a low-excitation, low-density component with $n < 10^4\,\mathrm{cm}^{-3}$ and a high-excitation, high-density component with $n > 3 \times 10^4\,\mathrm{cm}^{-3}$.

2. If we adopt the measured ammonia temperatures of Krieger et al. (2017) for these three clouds, assuming that the low-density gas has temperatures $T = 25$–60 K and the high-density gas has temperatures 60–100 K, we can further constrain the low-density component to be between 10^3 and 10^4 cm^{-3} and the high-density component to be between 8×10^4 and 4×10^5 cm^{-3}.

3. Comparing the relative columns of these two components, we find that all three clouds are consistent with having ~15% of the gas detected with HC$_3$N in the high-density component.

4. Across the entire CMZ, we find that the ratio of the HC$_3$N (10–9) to (3–2) line increases sharply at $R \lesssim 140$ pc. Based on the three clouds we modeled, we interpret this as indicating that the fraction of dense ($n > 10^4$ cm^{-3}) gas increases inward of this radius, consistent with the predictions of the model of Krumholz et al. (2017).

ORCID iDs

E. A. C. Mills ⦿ https://orcid.org/0000-0001-8782-1992
A. Ginsburg ⦿ https://orcid.org/0000-0001-6431-9633
A. Faure ⦿ https://orcid.org/0000-0002-8270-9907
M. R. Morris ⦿ https://orcid.org/0000-0002-6753-2066

References

Aalto, S., Monje, R., & Martín, S. 2007, A&A, 475, 479
Ao, Y., Henkel, C., Menten, K. M., et al. 2013, A&A, 550, A135
Araki, M., Takano, S., Sakai, N., et al. 2016, ApJ, 833, 291
Bally, J., Stark, A. A., Wilson, R. W., & Henkel, C. 1987, ApJS, 65, 13
Battersby, C., Bally, J., Ginsburg, A., et al. 2011, A&A, 535, A128
Belitsky, V., Lapkin, I., Fredrixon, M., et al. 2018, A&A, 612, A23
Binney, J., Gerhard, O. E., Stark, A. A., Bally, J., & Uchida, K. I. 1991, MNRAS, 252, 210
Blake, G. A., Sutton, E. C., Masson, C. R., & Phillips, T. G. 1987, ApJ, 315, 621
Boehle, A., Ghez, A. M., Schödel, R., et al. 2016, ApJ, 830, 1
Brown, P. D., Charnley, S. B., & Millar, T. J. 1988, MNRAS, 231, 409
Chapman, J. F., Millar, T. J., Wardle, M., Burton, M. G., & Walsh, A. J. 2009, MNRAS, 394, 221
Charnley, S. B., Tielens, A. G. G. M., & Millar, T. J. 1992, ApJL, 399, L71
Chomiuk, L., & Povich, M. S. 2011, AJ, 142, 197
Chou, R. C. Y., Peck, A. B., Lim, J., et al. 2007, ApJ, 670, 116
Clark, P. C., Glover, S. C. O., Ragan, S. E., Shetty, R., & Klessen, R. S. 2013, ApJL, 768, L34
Crocker, R. M. 2012, in Proc. IAU Symp., Vol. 284, The Spectral Energy Distribution of Galaxies, ed. R. J. Tuffs & C. C. Popescu (Cambridge: Cambridge Univ. Press), 371
Dahmen, G., Huttemeister, S., Wilson, T. L., & Mauersberger, R. 1998, A&A, 331, 959
de Vicente, P., Martín-Pintado, J., Neri, R., & Colom, P. 2000, A&A, 361, 1058
Elmegreen, D. M., Chromey, F. R., & Warren, A. R. 1998, AJ, 116, 2834
Etxaluze, M., Smith, H. A., Tolls, V., Stark, A. A., & González-Alfonso, E. 2011, AJ, 142, 134
Faure, A., Lique, F., & Wiesenfeld, L. 2016, MNRAS, 460, 2103
Federrath, C., Rathborne, J. M., Longmore, S. N., et al. 2016, ApJ, 832, 143
Fukuzawa, K., Osamura, Y., & Schaefer, H. F., III 1998, ApJ, 505, 278
García-Burillo, S., Martín-Pintado, J., Fuente, A., & Neri, R. 2000, A&A, 355, 499
Geballe, T. R., & Oka, T. 2010, ApJL, 709, L70
Ginsburg, A., Darling, J., Battersby, C., Zeiger, B., & Bally, J. 2011, ApJ, 736, 149
Ginsburg, A., Henkel, C., Ao, Y., et al. 2016, A&A, 586, A50
Gorski, M., Ott, J., Rand, R., et al. 2017, ApJ, 842, 124
Gorski, M., Ott, J., Rand, R., et al. 2018, ApJ, 856, 134
Goss, W. M., Schwarz, U. J., van Gorkom, J. H., & Ekers, R. D. 1985, MNRAS, 215, 69P
Goto, M., Usuda, T., Geballe, T. R., et al. 2011, PASJ, 63, L13
Goto, M., Usuda, T., Nagata, T., et al. 2008, ApJ, 688, 306
Güsten, R., & Henkel, C. 1983, A&A, 125, 136
Güsten, R., Walmsley, C. M., Ungerechts, H., & Churchwell, E. 1985, A&A, 142, 381
Henkel, C., Mauersberger, R., Peck, A. B., Falcke, H., & Hagiwara, Y. 2000, A&A, 361, L45
Henshaw, J. D., Longmore, S. N., Kruijssen, J. M. D., et al. 2016, MNRAS, 457, 2675
Hily-Blant, P., Faure, A., Vastel, C., et al. 2018, MNRAS, 480, 1174
Ho, P. T. P., Jackson, J. M., Barrett, A. H., & Armstrong, J. T. 1985, ApJ, 288, 575
Hüttemeister, S., Wilson, T. L., Bania, T. M., & Martin-Pintado, J. 1993, A&A, 280, 255
Imara, N. 2015, ApJ, 803, 38
Immer, K., Menten, K. M., Schuller, F., & Lis, D. C. 2012, A&A, 548, A120
Ishizuki, S., Kawabe, R., Ishiguro, M., et al. 1990, ApJ, 355, 436
Jones, P. A., Burton, M. G., Cunningham, M. R., et al. 2012, MNRAS, 419, 2961
Jones, P. A., Burton, M. G., Cunningham, M. R., Tothill, N. F. H., & Walsh, A. J. 2013, MNRAS, 433, 221
Kauffmann, J., Pillai, T., & Zhang, Q. 2013, ApJL, 765, L35
Kauffmann, J., Pillai, T., Zhang, Q., et al. 2017, A&A, 603, A89
Koepferl, C. M., Robitaille, T. P., Morales, E. F. E., & Johnston, K. G. 2015, ApJ, 799, 53
Krieger, N., Ott, J., Beuther, H., et al. 2017, ApJ, 850, 77
Kruijssen, J. M. D., Dale, J. E., & Longmore, S. N. 2015, MNRAS, 447, 1059
Kruijssen, J. M. D., Longmore, S. N., Elmegreen, B. G., et al. 2014, MNRAS, 440, 3370
Krumholz, M. R., & Kruijssen, J. M. D. 2015, MNRAS, 453, 739
Krumholz, M. R., Kruijssen, J. M. D., & Crocker, R. M. 2017, MNRAS, 466, 1213
Lada, C. J., Lombardi, M., Roman-Zuniga, C., Forbrich, J., & Alves, J. F. 2013, ApJ, 778, 133
Lahuis, F., & van Dishoeck, E. F. 2000, A&A, 355, 699
Lis, D. C., & Goldsmith, P. F. 1991, ApJ, 369, 157
Lis, D. C., Menten, K. M., Serabyn, E., & Zylka, R. 1994, ApJL, 423, L39
Lis, D. C., Pearson, J. C., Neufeld, D. A., et al. 2010a, A&A, 521, L9
Lis, D. C., Phillips, T. G., Goldsmith, P. F., et al. 2010b, A&A, 521, L26
Lis, D. C., Schilke, P., Bergin, E. A., Emprechtinger, M. & the HEXOS Team 2012, RSPTA, 370, 5162
Longmore, S. N., Bally, J., Testi, L., et al. 2013a, MNRAS, 429, 987
Longmore, S. N., Kruijssen, J. M. D., Bally, J., et al. 2013b, MNRAS, 433, L15
Longmore, S. N., Rathborne, J., Bastian, N., et al. 2012, ApJ, 746, 117
Lu, X., Zhang, Q., Kauffmann, J., et al. 2017, ApJ, 839, 1
Magnani, L., Zelenik, S., Dame, T. M., & Engebreth, B. 2006, ApJ, 636, 267
Martin, C. L., Walsh, W. M., Xiao, K., et al. 2004, ApJS, 150, 239
Mauersberger, R., Henkel, C., & Sage, L. J. 1990, A&A, 236, 63
Meier, D. S., & Turner, J. L. 2005, ApJ, 618, 259
Meier, D. S., & Turner, J. L. 2012, ApJ, 755, 104
Meier, D. S., Walter, F., Bolatto, A. D., et al. 2015, ApJ, 801, 63
Menten, K. M., Wyrowski, F., Belloche, A., et al. 2011, A&A, 525, A77
Mills, E. A. C., & Battersby, C. 2017, ApJ, 835, 76
Mills, E. A. C., Güsten, R., Requena-Torres, M. A., & Morris, M. R. 2013, ApJ, 779, 47
Mills, E. A. C., & Morris, M. R. 2013, ApJ, 772, 105
Molinari, S., Bally, J., Noriega-Crespo, A., et al. 2011, ApJL, 735, L33
Monje, R. R., Emprechtinger, M., Phillips, T. G., et al. 2011, ApJL, 734, L23
Montero-Castaño, M., Herrnstein, R. M., & Ho, P. T. P. 2009, ApJ, 695, 1477
Morris, M., Turner, B. E., Palmer, P., & Zuckerman, B. 1976, ApJ, 205, 82
Müller, H. S. P., Schlöder, F., Stutzki, J., & Winnewisser, G. 2005, JMoSt, 742, 215
Nagai, M., Tanaka, K., Kamegai, K., & Oka, T. 2007, PASJ, 59, 25
Nakanishi, H., & Sofue, Y. 2006, PASJ, 58, 847
Oka, T., Geballe, T. R., Goto, M., Usuda, T., & McCall, B. J. 2005, ApJ, 632, 882
Ott, J., Weiss, A., Henkel, C., & Walter, F. 2005, ApJ, 629, 767
Paglione, T. A. D., Jackson, J. M., Bolatto, A. D., & Heyer, M. H. 1998, ApJ, 493, 680

Paglione, T. A. D., Tosaki, T., & Jackson, J. M. 1995, ApJL, 454, L117
Rathborne, J. M., Longmore, S. N., Jackson, J. M., et al. 2015, ApJ, 802, 125
Requena-Torres, M. A., Güsten, R., Weiß, A., et al. 2012, A&A, 542, L21
Requena-Torres, M. A., Martin-Pintado, J., Rodríguez-Franco, A., et al. 2006, A&A, 455, 971
Riquelme, D., Amo-Baladrón, M. A., Martín-Pintado, J., et al. 2010, A&A, 523, A51
Riquelme, D., Bronfman, L., Mauersberger, R., et al. 2018, A&A, 610, A43
Schilke, P., Comito, C., Müller, H. S. P., et al. 2010, A&A, 521, L11
Serabyn, E., & Güsten, R. 1991, A&A, 242, 376
Serabyn, E., Lacy, J. H., & Achtermann, J. M. 1992, ApJ, 395, 166
Shetty, R., Beaumont, C. N., Burton, M. G., Kelly, B. C., & Klessen, R. S. 2012, MNRAS, 425, 720
Shirley, Y. L. 2015, PASP, 127, 299
Smith, I. L., & Wardle, M. 2014, MNRAS, 437, 3159
Sonnentrucker, P., Neufeld, D. A., Gerin, M., et al. 2013, ApJ, 763, L19
Sormani, M. C., Treß, R. G., Ridley, M., et al. 2018, MNRAS, 475, 2383
Suzuki, H., Yamamoto, S., Ohishi, M., et al. 1992, ApJ, 392, 551
Tanaka, K., Nagai, M., Kamegai, K., Iino, T., & Sakai, T. 2018, ApJS, 236, 40
van der Tak, F. F. S., Black, J. H., Schöier, F. L., Jansen, D. J., & van Dishoeck, E. F. 2007, A&A, 468, 627
Walmsley, C. M., Güsten, R., Angerhofer, P., Churchwell, E., & Mundy, L. 1986, A&A, 155, 129
Walsh, A. J., Breen, S. L., Britton, T., et al. 2011, MNRAS, 416, 1764
Wilson, T. L., & Rood, R. 1994, ARA&A, 32, 191
Yusef-Zadeh, F., et al. 2009, ApJ, 702, 178
Zylka, R., Guesten, R., Henkel, C., & Batrla, W. 1992, A&AS, 96, 525